Nanoscale Advances

ROYAL SOCIETY OF CHEMISTRY

PAPER

View Article Online
View Journal | View Issue

Cite this: *Nanoscale Adv.*, 2025, **7**, 3539

A facile two-step synthesis of hollow MOF-74 for enhanced dynamic Xe/Kr separation†

Chunhui Wu, *[ac] Xiaoling Wu, [ac] He Zhou,[a] Youshi Zeng,[a] Xinxin Chu,*[a] Wei Liu[ac] and Tao Li *[b]

Metal–organic frameworks (MOFs) with high-density uncoordinated open metal sites have been intensively investigated in Xe/Kr separation because of their strong and selective interaction with Xe. However, the dynamic Xe/Kr separation behavior of these MOFs is often unsatisfactory in practical applications due to slow diffusion kinetics. This work presents a facile two-step method to synthesize hollow Ni-MOF-74 particles with short diffusion lengths to enhance dynamic Xe/Kr separation. Unlike conventional sacrificial template approaches, where a crystalline MOF layer is directly grown on to the template surface, this method first rapidly deposits a metal–ligand complex layer under mild reaction conditions while the template undergoes simultaneous degradation. These poorly crystalline yet well-faceted hollow capsules are then reconstructed into crystalline hollow Ni-MOF-74 particles of the same morphology. Xe adsorption kinetics analyses show that the Xe diffusion rate of hollow Ni-MOF-74 was 1.5 times faster than that of solid Ni-MOF-74 despite their identical Xe and Kr adsorption capacity and selectivity. As a result, the enhanced diffusion kinetics of the hollow structure resulted in a steeper breakthrough curve and a 17% increase in breakthrough time than its solid counterpart during column separation of a Xe/Kr mixture.

Received 16th January 2025
Accepted 12th April 2025

DOI: 10.1039/d5na00064e

rsc.li/nanoscale-advances

Introduction

Xenon (Xe) and krypton (Kr) are important gases with significant industrial and medical applications, including imaging, anaesthesia and lighting for transport systems.[1–6] Traditionally, pure Xe and Kr are obtained through an energy extensive cryogenic distillation process.[7] In addition, the separation of Kr from Xe is a critical step in the removal of radioactive ^{85}Kr in nuclear waste remediation.[8,9] In contrast, physical adsorption can be carried out at room temperature with low regeneration energy consumption. As such, it is a more energy efficient and environmentally friendly alternative to separating Xe/Kr.[10] Many conventional porous materials, such as activated carbon, silica and zeolites, have been extensively studied for Xe/Kr separation. However, these materials typically exhibit low selectivity or adsorption capacities due to the lack of suitable pore sizes or specific adsorption sites for strong Xe/Kr interaction.[11–14]

Metal–organic frameworks (MOFs) are a class of inorganic–organic hybrid porous materials formed by self-assembly of organic ligands and metal ions or clusters that show great potential for adsorption-based gas separation due to their inherent properties such as high porosity, crystallinity and structural tunability.[15–26] MOF-74 is one of the classic MOFs which shows exceptional Xe/Kr separation properties due to the high-density uncoordinated open metal sites (OMSs) present in its 1-D hexagonal channels (Fig. S1†).[27–35] These OMSs contribute to a favourable interaction with Xe resulting in a Xe/Kr ideal selectivity of ~10.[35,36] However, the high static adsorption capacity of pure gases does not necessarily translate to practical dynamic Xe/Kr separation, as the diffusion kinetics of the adsorbate gas within the adsorbent plays a critical role.[37–41] Therefore, engineering the architecture of MOF materials to enhance the diffusion kinetics of gas molecules is essential for practical applications. Previously, it has been demonstrated that reducing the gas diffusion length in MOF crystals is an effective way to facilitate gas adsorption kinetics.[42–44]

Among various approaches, constructing hollow MOFs is an effective strategy to enhance gas adsorption kinetics because it shortens the diffusion pathway by introducing a large void within a particle. A common way to synthesize hollow MOFs is the sacrificial template approach, where the MOF is initially grown on the surface of a template such as ZIF-67,[45] UiO-66 (ref. 46) or polystyrene beads[47] followed by the template removal through dissolution or chemical etching.[48] The main challenge is that the sacrificial template needs to be stable enough to withstand the solvothermal growth conditions of the MOF shell, while also being easily removable without damaging the MOF

[a]*Shanghai Institute of Applied Physics, Chinese Academy of Sciences, Shanghai, China 201800. E-mail: wuchunhui@sinap.ac.cn; chuxinxin@sinap.ac.cn*

[b]*School of Physics, Chemistry and Earth Sciences, University of Adelaide, Adelaide, SA 5005, Australia. E-mail: tao.li@adelaide.edu.au*

[c]*Wuwei Institute of Advanced Energy, Gansu Province, China 733099*

† Electronic supplementary information (ESI) available. See DOI: https://doi.org/10.1039/d5na00064e

shell.[49] In addition, the harsh etching conditions for the removal of the template can often lead to defect formation in the shell.[50,51]

Herein, this work reports a facile two-step synthesis for the fabrication of polycrystalline hollow Ni-MOF-74 (denoted as Ni-MOF-74(h)) for improved dynamic Xe/Kr separation (Scheme 1). In the first stage, a metal–ligand complex (denoted as MLC) shell composed of Ni^{2+} and DOT was rapidly deposited on to the surface of a ZIF-8 template while the etching of ZIF-8 occurred at the same time. Since this deposition process does not involve crystallization, it is a much faster and simpler process in terms of synthetic conditions. A rapid deposition of the MLC is essential because it needs to form a rigid structure to contour the surfaces of ZIF-8 prior to its dissolution. In the second step, the MLC layer undergoes a ligand-assisted reconstruction (LAR) process, transforming into a crystalline Ni-MOF-74(h) under harsher synthetic conditions. In contrast to the conventional sacrificial template approaches, this method separates the surface deposition process from the crystallization process, thus circumventing the requirement of compatibility between the MOF growth condition and the template stability. When applied for Xe/Kr separation, the resultant Ni-MOF-74(h), with a 250 nm shell layer and a 1.3 μm cavity, exhibits a diffusion length that is 48% shorter than that of solid Ni-MOF-74. While both solid and Ni-MOF-74(h) exhibited identical Xe and Kr uptake capacity and Xe/Kr ideal selectivity, Ni-MOF-74(h) exhibited a steeper breakthrough curve and 17% increase in breakthrough time in a dynamic Xe/Kr separation experiment due to its faster gas adsorption kinetics.

Results and discussion

To construct Ni-MOF-74(h), monodispersed zeolitic imidazolate framework-8 (ZIF-8) with an average size of 1.3 μm was selected as a template (Fig. 1C, S2 and S3†).[52] A synthetic strategy previously developed by our group was adopted with minor modification to grow a polycrystalline Ni-MOF-74 shell on the surface of ZIF-8.[53] Next, 25, 50 or 100 mg ZIF-8 was added to the MOF-74 precursor solution (0.45 mmol $Ni(NO_3)_2 \cdot 6H_2O$, 0.05 mmol DOT, and 0.375 mL of 1 M NaOH aqueous) along with 5 eq. acetic acid (HOAc) with respect to DOT as a modulator to synthesize Ni-MOF-74(h). The mixture was heated at 100 °C in an oil bath for 30 min to yield a yellow solid product. As shown in Fig. S4,† the powder X-ray diffraction (PXRD) pattern of the product showed no diffraction peaks corresponding to ZIF-8, nor were the obvious characteristic peaks of MOF-74 observed. However, the transmission electron microscopy (TEM) images show that the reaction with the addition of 50 or 100 mg ZIF-8 led to hollow particles adopting the rhombic dodecahedral morphology of ZIF-8 particles. In contrast, the reaction with 25 mg ZIF-8 produced solid particle aggregates (Fig. 1A). Nevertheless, in all three cases, ZIF-8 was thoroughly dissolved by the acidic modulator. The product is likely a poorly crystalline phase composed of Ni^{2+} and DOC. We hereby denote this phase as MLC. Our previous study revealed that the synthesis of MOF-74 is highly sensitive to the pH value and the crystalline product was only formed in a narrow pH range (8.63–9.55).[44] During the reaction, the etching process of ZIF-8 consumed protons from DOT, elevating the pH value (Fig. S5†), which accelerated the deposition of the MLC. Note that the elevated pH is crucial for slowing the etching of ZIF-8, allowing sufficient time for the complete deposition of the MLC. The average thickness of the hollow shell decreased accordingly from ~320 nm to ~220 nm with ZIF-8 increased from 50 to 100 mg. It is also noted that 100 mg ZIF-8 produced the most well-defined hollow structure possibly due to the slow dissolution of the sacrificial template. Therefore, this reaction condition was used as the basis for further optimization.

To further understand the mechanism of MLC deposition, zeta potential measurement was carried out for ZIF-8 before and after incubation with a DOT solution. The surface charge of the pristine ZIF-8 was found to be 24.53 mV. After incubating with DOT, the zeta potential shifted to −5.03 mV (Fig. S6†). This is likely due to surface adsorption of negatively charged deprotonated DOT. The enrichment of DOT on ZIF-8 surfaces is the driving force for the rapid deposition of the MLC.

Next, the amount of HOAc was changed from 5 to 15 eq. with respect to DOT. As shown in Fig. 1B and S7,† increasing the concentration of HOAc resulted in less defined hollow morphology due to rapid etching of ZIF-8 disrupting the formation of the MLC. When 15 eq. HOAc was applied, no hollow structure was observed (Fig. 1B(iii)).[54] From here on, 5 eq. HOAc was used in all reactions. Scanning electron microscopy (SEM) images show that hollow MLC particles manifest a clear ZIF-8-like dodecahedral morphology with a wrinkled surface texture (Fig. 1D). Energy dispersive X-ray spectroscopy (EDS) mapping and line scan results revealed that the Ni signal is uniformly distributed throughout the hollow shell (Fig. 2A). It is noted that the Zn signal was also detected, suggesting the presence of residual Zn in the hollow MLC after etching. Moreover, the shape and size of the hollow cavity can also be adjusted by regulating the size and shape of the template. As shown in Fig. 2C, cubic-shaped MLC particles featuring ~200 nm cavities were obtained by using cubic ZIF-8 as the template (Fig. 2B and S8†).

The porosity of the hollow MLC was studied by N_2 adsorption experiments (77 K) (Fig. 2D). ZIF-8 shows a pore volume and Brunauer–Emmett–Teller (BET) surface area of 0.656 $cm^3\ g^{-1}$ and 2581 $m^2\ g^{-1}$, respectively, higher than that of solid Ni-MOF-74 (0.42 $cm^3\ g^{-1}$ and 1076 $m^2\ g^{-1}$), due to its 3-D porous topology as opposed to the 1-D porous structure of Ni-MOF-74 (Fig. S1†). The hollow MLC exhibits a BET surface area of 406 $m^2\ g^{-1}$, which is only 38% of that of solid Ni-MOF-74 and 16%

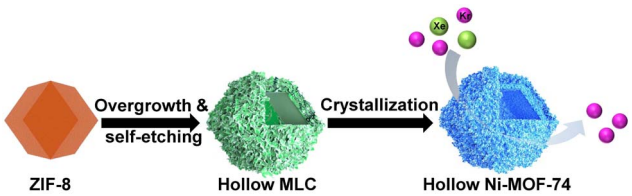

Scheme 1 Hollow Ni-MOF-74 was synthesized by a two-step process to enhance the dynamic separation of Xe/Kr.

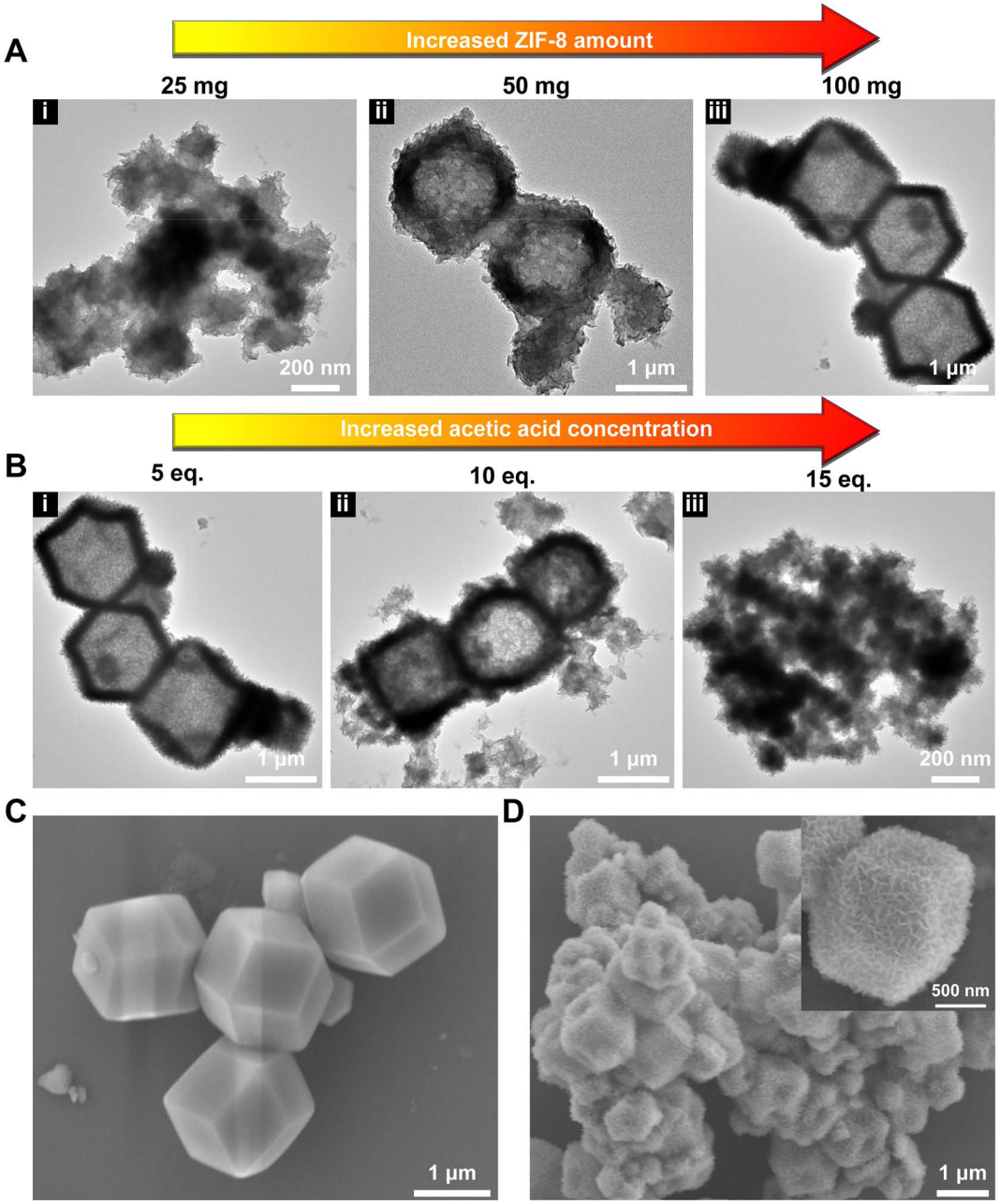

Fig. 1 (A) TEM images of the hollow MLC synthesized with various amounts of ZIF-8. (B) TEM images of the hollow MLC synthesized with various amounts of HOAc. SEM images of dodecahedral ZIF-8 (C) and the hollow MLC (D).

of that of ZIF-8 (Table S1†). Meanwhile, the pore-size distribution analysis shows that there is almost no micropore present in the hollow MLC (Fig. 2E), confirming its poor crystallinity.

To carry out LAR, the hollow MLC was dispersed in a DMF solution of DOT and heated to 120 °C for 12 h to yield Ni-MOF-74(h). TEM and SEM images show that the surface of Ni-MOF-74(h) became more granular with the average shell thickness increased slightly from ~220 nm for the hollow MLC particles to ~250 nm (Fig. 3A, B, S9 and S10†). The PXRD pattern of Ni-MOF-74(h) perfectly matches with the pattern simulated from the Ni-MOF-74 crystal structure, confirming its phase purity and high crystallinity (Fig. 3C). Meanwhile, peak broadening is observed for Ni-MOF-74(h) due to the small crystallite size. The average crystallite size of Ni-MOF-74 calculated from the Scherrer equation (eqn (S1)†) is ~25 nm, an order of magnitude smaller than the shell thickness of Ni-MOF-74(h).

The elemental composition and electronic state of Ni-MOF-74(h) were analyzed by X-ray photoelectron spectroscopy (XPS). The presence of N and Zn signals in the XPS survey spectrum indicates that there are still residual Zn(II) and 2-methylimidazole in Ni-MOF-74(h) (Fig. S11†). The peaks at 285.1 eV, 531.2 eV and 855.8 eV can be attributed to C 1s, O 1s, and Ni 2p, respectively (for details see the ESI†). Notably, the peaks at 530.6 eV in O 1s are assigned to Ni–O, indicating the

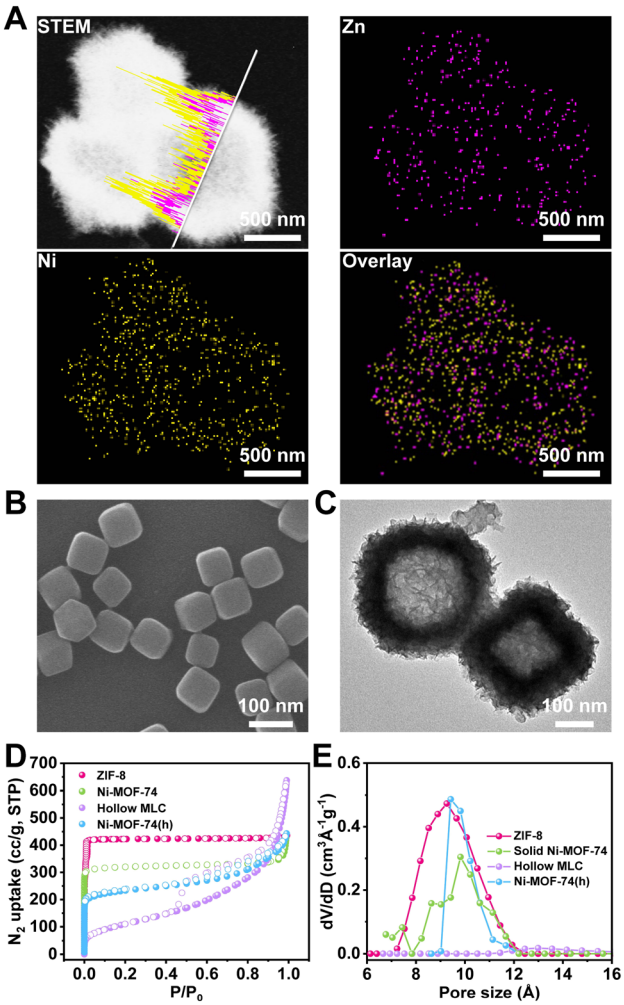

Fig. 2 (A) STEM, EDS elemental mapping images and line scan patterns of the hollow MLC. (B) SEM image of cubic ZIF-8. (C) TEM images of the hollow MLC with a cubic cavity. (D) N_2 adsorption–desorption isotherms at 77 K of ZIF-8, solid Ni-MOF-74, the hollow MLC and solid Ni-MOF-74(h). (E) Pore size distribution of ZIF-8, solid Ni-MOF-74, the hollow MLC and Ni-MOF-74(h).

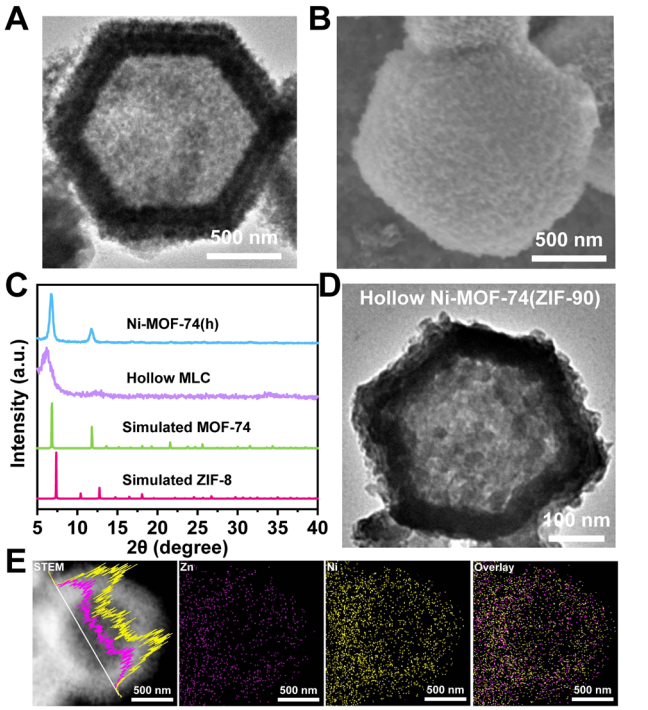

Fig. 3 SEM (A) and TEM (B) images of Ni-MOF-74(h). (C) PXRD patterns of the hollow MLC and Ni-MOF-74(h). (D) TEM image of Ni-MOF-74(h) by using ZIF-90 as the template. (E) STEM, EDS elemental mapping images and line scan patterns of Ni-MOF-74(h).

complexation between Ni(II) and O. Fourier transform infrared spectroscopy (FTIR) was then carried out to examine the functionality of Ni-MOF-74(h). As shown in Fig. S12,† all the characteristic peaks of DOT are available in the FTIR spectrum of Ni-MOF-74(h) (for details see the ESI†). Two absorption peaks appearing at 889 cm^{-1} and 814 cm^{-1} corresponded to C–O–Ni vibration.[55] Moreover, the peak at 1140 cm^{-1} can be assigned to C–N stretching vibration, which further confirm the presence of residual 2-methylimidazole in Ni-MOF-74(h).

The N_2 adsorption isotherms of Ni-MOF-74(h) at 77 K were collected to investigate its porosity. The BET surface area of Ni-MOF-74(h) was calculated to be 885 $m^2\ g^{-1}$ which is more than twice that of the hollow MLC (406 $m^2\ g^{-1}$) (Fig. 2D and Table S1†) yet slightly lower than that of solid Ni-MOF-74 (1076 $m^2\ g^{-1}$). A similar trend was also found in CO_2 adsorption isotherms at 298 K, where Ni-MOF-74(h) and solid Ni-MOF-74 adsorbed 121 and 141 cc per g CO_2, respectively, at 1 bar (Fig. S13†). This slight discrepancy in the BET surface area and CO_2 uptake capacity is likely due to non-porous Zn(II) and 2-methylimidazole residues that either took up part of the sample weight or occupied the pores of Ni-MOF-74(h). This hypothesis is again supported by the EDS elemental mapping, FTIR and XPS results (Fig. 3E, S11 and S12†). The pore size distribution of Ni-MOF-74(h) shows the presence of micropores in the range from 9 to 12 Å which is consistent with that of solid Ni-MOF-74 (Fig. 2E). All the results confirm that the transformation of hollow MLC to Ni-MOF-74(h) was successful and complete. Moreover, using the two-step method, Ni-MOF-74(h) also can be synthesized by using 345 nm ZIF-90 particles as a template leading to a much smaller hollow structure with an average size of 397 nm and shell thickness of 52 nm (Fig. 3D and S14†).

Next, we turned to investigate Xe and Kr adsorption and separation behaviors of Ni-MOF-74(h). The synthesized solid Ni-MOF-74 rods were used as a control sample to compare with Ni-MOF-74(h) (Fig. S15†).[44] The SEM images show that the average length of the solid Ni-MOF-74 bulk rod is 958 nm (Fig. S16†). Xe and Kr adsorption isotherms of Ni-MOF-74(h) and solid Ni-MOF-74 at 298 K were collected and compared to investigate the effect of morphology on Xe/Kr adsorption and separation behaviors (Fig. 4A). In general, both samples have a stronger affinity for Xe than for Kr due to the high-density unsaturated Ni(II) sites present in Ni-MOF-74.[56] Fig. 4A shows that Ni-MOF-74(h) achieved slightly higher Xe and Kr uptake capacities at 118 cc g^{-1} and 29 cc g^{-1}, respectively, at 298 K, 1 bar compared to that of solid Ni-MOF-74 (96.7 cc g^{-1} and 20.2 $m^2\ g^{-1}$,

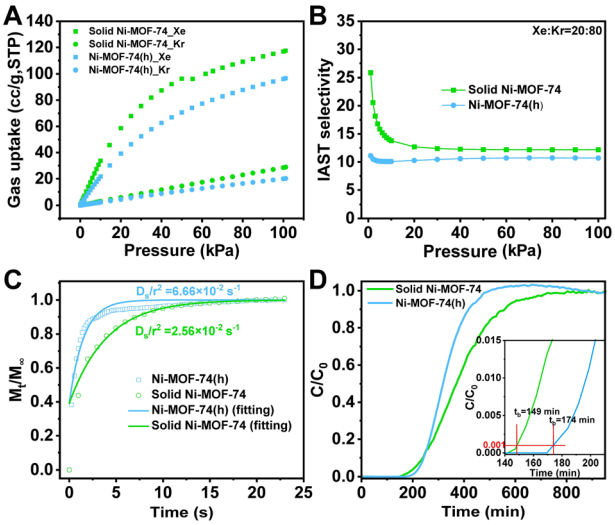

Fig. 4 (A) Kr and Xe adsorption isotherms at 298 K of solid Ni-MOF-74 and Ni-MOF-74(h). (B) Calculated IAST selectivity for a Xe/Kr mixture (v/v = 20/80) of solid Ni-MOF-74 and Ni-MOF-74(h) at 298 K. (C) Kinetic curves of Xe uptake for solid Ni-MOF-74 and Ni-MOF-74(h) at 298 K (P/P_0 = 0.03). The solid line shows the fitting curves using the Fickian diffusion model. (D) Column breakthrough curves of Xe for solid Ni-MOF-74 and Ni-MOF-74(h) at 1 atm, 298 K using a Kr/Xe/Ar mixture (Xe 20 ppm, Kr 3.3 ppm, Ar > 99.999%).

respectively). The discrepancy in Xe and Kr uptake capacities is likely due to the residual non-porous Zn(II) and 2-methyl imidazole residing within Ni-MOF-74(h) (Fig. 3E, S11 and S12†). Using the ideal adsorbed solution theory (IAST), the separation selectivity of a 20 : 80 Xe–Kr binary gas mixture at 298 K, 1 bar was predicted to be 10.7 for Ni-MOF-74(h) and 12.2 for solid Ni-MOF-74 using experimental pure gas adsorption isotherms (Fig. 4B, S17 and eqn (S3)†).[57] These results indicate that the polycrystallinity of Ni-MOF-74(h) has no major negative impact on the Xe and Kr sorption and separation.

A pressure decay approach was used to investigate the kinetics of gas adsorption (Fig. S18†). The kinetic gas uptake curves were fitted to calculate D_s/r^2 values (D_s/r^2 represents the gas adsorption rate, where D_s is the diffusion coefficient and r is the diffusion length) by using the constant surface concentration model (also known as the Fickian diffusion model) (eqn (S4)†).[58] As shown in Fig. 4C, Ni-MOF-74(h) shows a steeper initial pressure change suggesting a faster adsorption kinetics at P/P_0 = 0.03. The D_s/r^2 value of Ni-MOF-74(h) is calculated to be 6.66 × 10^{-2} s^{-1}, 1.5 times faster than that of solid Ni-MOF-74 (2.56 × 10^{-2} s^{-1}). This improvement can be attributed to the shorter gas diffusion distance (~250 nm) of Ni-MOF-74(h) compared to solid Ni-MOF-74 (~479 nm). It is also possible that the defects at the grain boundary of polycrystalline Ni-MOF-74 can also contribute positively to diffusion. It is thus reasonable to conclude that shortening the gas diffusion distance of Ni-MOF-74 to form a hollow structure led to a faster Xe and Kr adsorption kinetics without compromising Xe and Kr uptake capacity and selectivity.

To further investigate the dynamic Xe/Kr separation performance of Ni-MOF-74(h), the breakthrough experiment was carried out in a fixed bed column with a gas mixture (Xe 20 ppm, Kr 3.3 ppm, Ar > 99.999%) at 1 atm, 298 K, which simulates the real off-gas treatment system in a Thorium-based Molten Salt Reactor with Liquid Fuel (TMSR-LF) designed by the Shanghai Institute of Applied Physics (Fig. S19†).[59] The breakthrough experiment was performed in a packed column (φ 4 mm inner diameter, 11 cm length) with a total flow of 1 cm^3 min^{-1}. As shown in Fig. 4D, the breakthrough curves of Ni-MOF-74(h) and solid Ni-MOF-74 were obtained. Both solid Ni-MOF-74 and Ni-MOF-74(h) can effectively separate Xe from Kr due to their strong affinity for Xe over Kr. The total Xe adsorption capacity calculated from the breakthrough curves is 2.9 and 3.5 mmol kg^{-1} for Ni-MOF-74(h) and solid Ni-MOF-74, respectively, which demonstrates that the hollow structure has no negative effect on the dynamic adsorption capacity (eqn (S5)†). However, Ni-MOF-74(h) exhibits a steeper breakthrough curve than that of solid Ni-MOF-74 due to faster adsorption kinetics. In this work, the breakthrough time (t_b) was arbitrarily defined as the time when C/C_0 reached 0.1%. The t_b of solid Ni-MOF-74(h) is 174 min, 17% longer than that of solid Ni-MOF-74 (149 min) (Fig. 4D). This indicates that reducing the gas diffusion distance to form the hollow structure can improve diffusion kinetics leading to a higher working capacity during dynamic Xe/Kr separation performance.

Conclusions

In summary, a simple two-step method was developed to successfully synthesize hollow, rhombic dodecahedron-shaped Ni-MOF-74 particles. This synthetic approach decouples the surface deposition from the crystallization process, making the sacrificial template method applicable to a broader range of hollow MOF syntheses. The shorter diffusion length in Ni-MOF-74(h) resulted in 1.5 times faster adsorption kinetics compared to its solid counterpart, leading to a steeper breakthrough curve and a 17% increase in breakthrough time during dynamic column Xe/Kr separation. The method proposed in this work offers a potential general approach to enhancing the dynamic gas separation performance of MOF materials.

Data availability

The authors confirm that the data supporting the findings of this study are available within the article and its ESI.†

Conflicts of interest

There are no conflicts to declare.

Acknowledgements

This work was supported by the Gansu Major Scientific, Technological Special Project (Grant No. 23ZDGH001), the Natural Science Foundation of Gansu Province, China (Grant No. 23JRRH0009), Wuwei Institute of Advanced Energy, the Young Scientists Fund of the National Natural Science Foundation of China (Grant No. 22405288) and the Youth Innovation

Promotion Association, Chinese Academy of Sciences (Grant No. 2021254).

Notes and references

1 A. K. Chhandak, R. Israni and A. Trivedi, *Int. J. Curr. Microbiol. Appl. Sci.*, 2017, **6**, 2063–2068.
2 S. C. Cullen and E. G. Gross, *Science*, 1951, **113**, 580–582.
3 G. A. Lane, M. L. Nahrwold, A. R. Tait, M. Taylor-Busch, P. J. Cohen and A. R. Beaudoin, *Science*, 1980, **210**, 899–901.
4 J. Marshall and A. C. Bird, *Br. J. Ophthalmol.*, 1979, **63**, 657–668.
5 P. Chuong and N. Xuan, *Determination of Partial Pressure Ratio of Krypton and Argon in the Mixture of Gases Inserted in Fluorescent Lamps*, National Inst. for Nuclear Research, 1989.
6 G. E. Pavlovskaya, Z. I. Cleveland, K. F. Stupic, R. J. Basaraba and T. Meersmann, *Proc. Natl. Acad. Sci. U. S. A.*, 2005, **102**, 18275–18279.
7 F. G. Kerry, *Industrial Gas Handbook: Gas Separation and Purification*, CRC Press, 2007.
8 S. U. Nandanwar, K. Coldsnow, V. Utgikar, P. Sabharwall and D. E. Aston, *Chem. Eng. J.*, 2016, **306**, 369–381.
9 N. R. Soelberg, T. G. Garn, M. R. Greenhalgh, J. D. Law, R. Jubin, D. M. Strachan and P. K. Thallapally, *Sci. Technol. Nucl. Install.*, 2013, **2013**, 702496.
10 J. P. Fraissard, *Physical Adsorption: Experiment, Theory, and Applications*, Springer Science & Business Media, 1997.
11 C. G. Saxton, A. Kruth, M. Castro, P. A. Wright and R. F. Howe, *Microporous Mesoporous Mater.*, 2010, **129**, 68–73.
12 C. J. Jameson, A. K. Jameson and H.-M. Lim, *J. Chem. Phys.*, 1997, **107**, 4364–4372.
13 R. Bazan, M. Bastos-Neto, A. Moeller, F. Dreisbach and R. Staudt, *Adsorption*, 2011, **17**, 371–383.
14 K. Munakata, T. Fukumatsu, S. Yamatsuki, K. Tanaka and M. Nishikawa, *J. Nucl. Appl. Technol.*, 1999, **36**, 818–829.
15 O. K. Farha and J. T. Hupp, *Acc. Chem. Res.*, 2010, **43**, 1166–1175.
16 O. M. Yaghi, M. O'Keeffe, N. W. Ockwig, H. K. Chae, M. Eddaoudi and J. Kim, *Nature*, 2003, **423**, 705–714.
17 K. Sumida, D. L. Rogow, J. A. Mason, T. M. McDonald, E. D. Bloch, Z. R. Herm, T.-H. Bae and J. R. Long, *Chem. Rev.*, 2011, **112**, 724–781.
18 S. M. Cohen, *Chem. Rev.*, 2011, **112**, 970–1000.
19 H.-C. Zhou, J. R. Long and O. M. Yaghi, *Chem. Rev.*, 2012, **112**, 673–674.
20 H. Furukawa, K. E. Cordova, M. O'Keeffe and O. M. Yaghi, *Science*, 2013, **341**, 1230444.
21 S. Kitagawa, *Chem. Soc. Rev.*, 2014, **43**, 5415–5418.
22 G. Maurin, C. Serre, A. Cooper and G. Férey, *Chem. Soc. Rev.*, 2017, **46**, 3104–3107.
23 L. Li, R.-B. Lin, R. Krishna, H. Li, S. Xiang, H. Wu, J. Li, W. Zhou and B. Chen, *Science*, 2018, **362**, 443–446.
24 A. Cadiau, K. Adil, P. Bhatt, Y. Belmabkhout and M. Eddaoudi, *Science*, 2016, **353**, 137–140.
25 J. A. Mason, K. Sumida, Z. R. Herm, R. Krishna and J. R. Long, *Energy Environ. Sci.*, 2011, **4**, 3030–3040.
26 Y. Yang, C. Tu, L. Guo, L. Wang, F. Cheng and F. Luo, *Cell Rep. Phys. Sci.*, 2023, **4**, 101694.
27 N. L. Rosi, J. Kim, M. Eddaoudi, B. Chen, M. O'Keeffe and O. M. Yaghi, *J. Am. Chem. Soc.*, 2005, **127**, 1504–1518.
28 S. R. Caskey, A. G. Wong-Foy and A. J. Matzger, *J. Am. Chem. Soc.*, 2008, **130**, 10870–10871.
29 P. D. Dietzel, R. E. Johnsen, R. Blom and H. Fjellvåg, *Chem.–Eur. J.*, 2008, **14**, 2389–2397.
30 S. Bhattacharjee, J.-S. Choi, S.-T. Yang, S. B. Choi, J. Kim and W.-S. Ahn, *J. Nanosci. Nanotechnol.*, 2010, **10**, 135–141.
31 Q. Zhang, B. Li and L. Chen, *Inorg. Chem.*, 2013, **52**, 9356–9362.
32 M. J. Katz, A. J. Howarth, P. Z. Moghadam, J. B. DeCoste, R. Q. Snurr, J. T. Hupp and O. K. Farha, *Dalton Trans.*, 2016, **45**, 4150–4153.
33 P. A. Julien, K. Užarević, A. D. Katsenis, S. A. Kimber, T. Wang, O. K. Farha, Y. Zhang, J. Casaban, L. S. Germann and M. Etter, *J. Am. Chem. Soc.*, 2016, **138**, 2929–2932.
34 Y. Tao, Y. Fan, Z. Xu, X. Feng, R. Krishna and F. Luo, *Inorg. Chem.*, 2020, **59**, 11793–11800.
35 T. Vazhappilly, T. K. Ghanty and B. Jagatap, *J. Phys. Chem. C*, 2016, **120**, 10968–10974.
36 J. Liu, P. K. Thallapally and D. Strachan, *Langmuir*, 2012, **28**, 11584–11589.
37 K. Li, D. H. Olson, J. Seidel, T. J. Emge, H. Gong, H. Zeng and J. Li, *J. Am. Chem. Soc.*, 2009, **131**, 10368–10369.
38 C. Y. Lee, Y.-S. Bae, N. C. Jeong, O. K. Farha, A. A. Sarjeant, C. L. Stern, P. Nickias, R. Q. Snurr, J. T. Hupp and S. T. Nguyen, *J. Am. Chem. Soc.*, 2011, **133**, 5228–5231.
39 K. Hirai, J. Reboul, N. Morone, J. E. Heuser, S. Furukawa and S. Kitagawa, *J. Am. Chem. Soc.*, 2014, **136**, 14966–14973.
40 J. Peng, H. Wang, D. H. Olson, Z. Li and J. Li, *Chem. Commun.*, 2017, **53**, 9332–9335.
41 Y. Wang and D. Zhao, *Cryst. Growth Des.*, 2017, **17**, 2291–2308.
42 H. Uehara, S. Diring, S. Furukawa, Z. Kalay, M. Tsotsalas, M. Nakahama, K. Hirai, M. Kondo, O. Sakata and S. Kitagawa, *J. Am. Chem. Soc.*, 2011, **133**, 11932–11935.
43 X. Zhang, C. Y. Chuah, P. Dong, Y.-H. Cha, T.-H. Bae and M.-K. Song, *ACS Appl. Mater. Interfaces*, 2018, **10**, 43316–43322.
44 C. Wu, L.-Y. Chou, L. Long, X. Si, W.-S. Lo, C.-K. Tsung and T. Li, *ACS Appl. Mater. Interfaces*, 2019, **11**, 35820–35826.
45 X. Y. Liu, F. Zhang, T. W. Goh, Y. Li, Y. C. Shao, L. Luo, W. Huang, Y. T. Long, L. Y. Chou and C. K. Tsung, *Angew. Chem., Int. Ed.*, 2018, **57**, 2110–2114.
46 C. Wu, X. Zhao, D. Wang, X. Si and T. Li, *Chem. Sci.*, 2022, **13**, 13338–13346.
47 H. J. Lee, W. Cho and M. Oh, *Chem. Commun.*, 2012, **48**, 221–223.
48 T. Qiu, S. Gao, Z. Liang, D. G. Wang, H. Tabassum, R. Zhong and R. Zou, *Angew. Chem., Int. Ed.*, 2021, **60**, 17314–17336.
49 D. Liu, J. Wan, G. Pang and Z. Tang, *Adv. Mater.*, 2019, **31**, 1803291.

50 X. Liu, G. Verma, Z. Chen, B. Hu, Q. Huang, H. Yang, S. Ma and X. Wang, *Innovation*, 2022, **3**, 100281.
51 X. Wang, J. Feng, Y. Bai, Q. Zhang and Y. Yin, *Chem. Rev.*, 2016, **116**, 10983–11060.
52 Q. Shi, Z. Chen, Z. Song, J. Li and J. Dong, *Angew. Chem., Int. Ed.*, 2011, **50**, 672–675.
53 C. Wu, K. Zhang, H. Wang, Y. Fan, S. Zhang, S. He, F. Wang, Y. Tao, X. Zhao and Y.-B. Zhang, *J. Am. Chem. Soc.*, 2020, **142**, 18503–18512.
54 S. Gao, J. Hou, Z. Deng, T. Wang, S. Beyer, A. G. Buzanich, J. J. Richardson, A. Rawal, R. Seidel and M. Y. Zulkifli, *Chem*, 2019, **5**, 1597–1608.
55 P. Huang, X. Wang, J. Zhao, Z. Zhang, X. Du and X. Lu, *Chem. Eng. J.*, 2022, **449**, 137759.
56 S.-J. Lee, K. C. Kim, T.-U. Yoon, M.-B. Kim and Y.-S. Bae, *Microporous Mesoporous Mater.*, 2016, **236**, 284–291.
57 A. L. Myers and J. M. Prausnitz, *AIChE J.*, 1965, **11**, 121–127.
58 D. D. Do, *Adsorption Analysis: Equilibria and Kinetics*, Imperial College Press, London, 1998.
59 Z. Dai, *Thorium Molten Salt Reactor Nuclear Energy System*, Elsevier, 2017, pp. 803–814.